IEEE Access
Multidisciplinary | Rapid Review | Open Access Journal

Received 17 January 2024, accepted 5 February 2024, date of publication 14 February 2024, date of current version 23 February 2024.

Digital Object Identifier 10.1109/ACCESS.2024.3366345

RESEARCH ARTICLE

Radial Displacement Measurement Method in Bearingless Slice Motor Through Eddy Current Displacement Sensors Positioned on the Underside of the Rotor

REN YANG[1], ZEQIANG HE[1], (Graduate Student Member, IEEE), NAOHIRO SUGITA[2], AND TADAHIKO SHINSHI[2], (Member, IEEE)

[1]Department of Mechanical Engineering, Tokyo Institute of Technology, Yokohama 226-8503, Japan
[2]Institute of Innovative Research, Tokyo Institute of Technology, Yokohama 226-8503, Japan

Corresponding author: Tadahiko Shinshi (shinshi.t.ab@m.titech.ac.jp)

This work was supported in part by Tsugawa Foundation.

ABSTRACT Bearingless slice motors (BELSM) employing active radial positioning control and passive stabilization in the axial and tilt directions are widely utilized in medical and industrial applications. Conventionally, the radial displacement of a BELSM is measured by arranging eddy current displacement (ECD) sensors either outside or inside the rotor to detect its radial movement. However, this sensor placement method either increases the rotor's height because of an additional sensor target or occupies the inner space because of the sensor holder. To address this issue, we propose the mounting of ECD sensors on the underside of the inner edge of the rotor for radial displacement measurements. However, formulating the radial displacement from the sensor outputs is challenging because of complex sensor nonlinearities and the effects of axial movement and tilt. To resolve this problem, we propose the usage of seven ECD sensor placements and establish relationships between the sensor outputs and radial displacement. Initially, displacement estimation based on the polynomial fitting method is proposed, however, it results in unacceptable measurement errors owing to sensor calibration errors. Subsequently, a neural network (NN) method is proposed, which exhibits good linearity within ± 150 μm and a measurement bandwidth of up to 200 Hz. The NN is further implemented into the displacement feedback system, enabling magnetic suspension startup and rotation with a radial displacement measurement error controlled within 16 μm within 1700 rpm. Diverse and large datasets, coupled with an increased number of sensors can substantially enhance measurement accuracy.

INDEX TERMS Bearingless slice motor, magnetic suspension, eddy current displacement sensor, radial displacement measurement, neural network.

NOMENCLATURE

x	Radial displacement of the rotor in the X-direction.
y	Radial displacement of the rotor in the Y-direction.
z	Axial displacement of the rotor.
H_R	The height of the rotor.
D_s	The diameter of the ECD sensor probe.
H_s	The axial initial installation distance between the sensor probe and rotor bottom surface.
d	The inner diameter of the rotor.
D	The outer diameter of the rotor.
g_s	The radial initial installation distance between the sensor probe and rotor side surface.
θ_x	Tilt angle around the X-axis.

The associate editor coordinating the review of this manuscript and approving it for publication was Jinquan Xu.

θ_y	Tilt angle around the Y-axis.
S_i	ECD sensors located at the center of the bottom of the rotor circular ring (i = 1-3).
S_j	ECD sensors located at the inner edge of the rotor bottom parallel to the X- and Y-axes (j = 4-7).
V_i, V_j	Output voltages of the S_i and S_j.
G_i, G_j	The axial distance between the rotor bottom surface and sensor probes of the S_i and S_j.
u_i	The polynomial functions of V_i to establish the relationship with the G_i.
α_{il}	The coefficient of each polynomial term for u_i.
R_c	The radial distance between the centerlines of sensor probes S_i and the rotor.
k_j	The polynomial functions of G_j to calculate the slope of the fitted linear equation.
b_j	The polynomial functions of G_j to calculate the intercept of the fitted linear equation.
β_{jl}	The coefficients of each polynomial term for k_j.
γ_{jl}	The coefficient of each polynomial term for b_j.
N_n	The total input of the nth neuron in the current layer from the preceding layer.
p, c	The number of neurons in the preceding and current layers, respectively.
w_{nm}	The weight of the connection from the mth neuron in the preceding layer to the nth in the current layer.
B_n	The bias values of the nth neuron in the current layer.
a_n	The nth neuron output in the current layers.
a_m	The mth neuron output in the preceding layers.
g	The appropriate activation function.
Δw_{nm}	The weight correction terms.
ΔB_n	The bias correction terms.
E	The mean square error.
$\hat{B}_n$	The updated bias value of the nth neuron in the current layer.
$\hat{w}_{nm}$	The updated weight from the mth neuron in the preceding layer to the nth in the current layer.
η	The learning rate parameter.

I. INTRODUCTION

Bearingless motor technology is a cutting-edge solution that integrates an electromagnetic motor and magnetic bearing on the same stator and rotor, permitting rotor rotation with no mechanical bearing support. This technology simplifies the mechanism, enabling high rotational speed operation, hermetically sealing the rotor from the stator for operation in high-purity or harsh environments, and reducing shear stress as well as heat generation, making it suitable for use in the medical and industrial fields [1], [2], [3], [4], [5], [6], [7], [8].

The bearingless slice motor (BELSM) concept has been proposed to reduce the system complexity and number of required sensors [9], [10], which features a slice rotor with a diameter that is considerably larger than its height. The slice rotor can be passively supported in the tilt and axial directions through a robust magnetic coupling in the lateral air gap. The electromagnets actively control only two of the degrees of freedom (DOFs) in the radial direction. This design provides a simple structure in the centrifugal blood pump (CBP) application [11], [12]. It offers sufficient torque to generate the required flow and pressure while utilizing contactless support, which enhances biocompatibility and durability. Moreover, this design allows the thin rotor to reduce the size of the pump head and minimize the initial filling volume in the CBP. Fig. 1 (a) shows a photograph of CBP utilizing BELSM, developed by our group [3], and Fig. 1 (b) shows the side cross-section view of the BELSM with a disposable pump head. The disposable pump head comprises the pump housing and integrated slice rotor/impeller, while the motor body encompasses the stator, slice rotor, and coils.

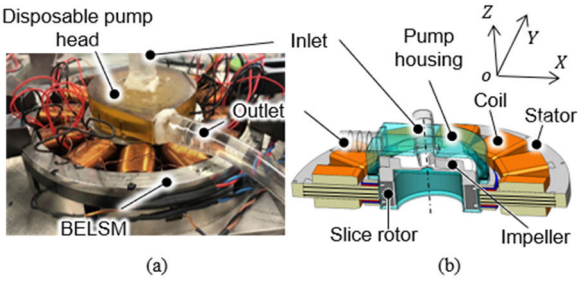

FIGURE 1. (a) Photograph of CBP utilizing the BELSM developed by our group; (b) Side cross-section view of the BELSM with a disposable pump head.

Accurate radial displacement information is crucial to achieving precise radial positioning feedback control of slice rotors. Placing eddy current displacement (ECD) sensors against the inside or outside of the rotor is a standard method to measure the radial displacement of a BELSM rotor for CBP in liquids, as shown in Figs. 2 (a) and (b) [13], [14], [15], [16], [17], where light penetration for laser displacement measurement is challenging. The ECD sensors are required to face the high roundness, the nonsalient, and the no-tooth side surface of the rotor to detect the radial displacement of the rotor, and the side surface is referred to as a sensor target. Usually, the sensor target is the inside or outside surface of the rotor. ECD sensors have a high measurement bandwidth, which is advantageous for real-time measurement of rotor displacement and for designing high-performance suspension control systems. The carrier frequency of the ECD sensor is considerably higher than the frequencies of the suspension and motor current, which helps prevent coupling between the sensor and electrical drive systems as well as ensures high measurement accuracy and reliability.

However, in the ongoing development of the bearingless reluctance slice motor (BELRSM), the slice rotor is designed with salient poles on its outer circumference. The salient poles on the outer side of the slice rotor make it challenging to provide a sensor target independent of the rotor angle

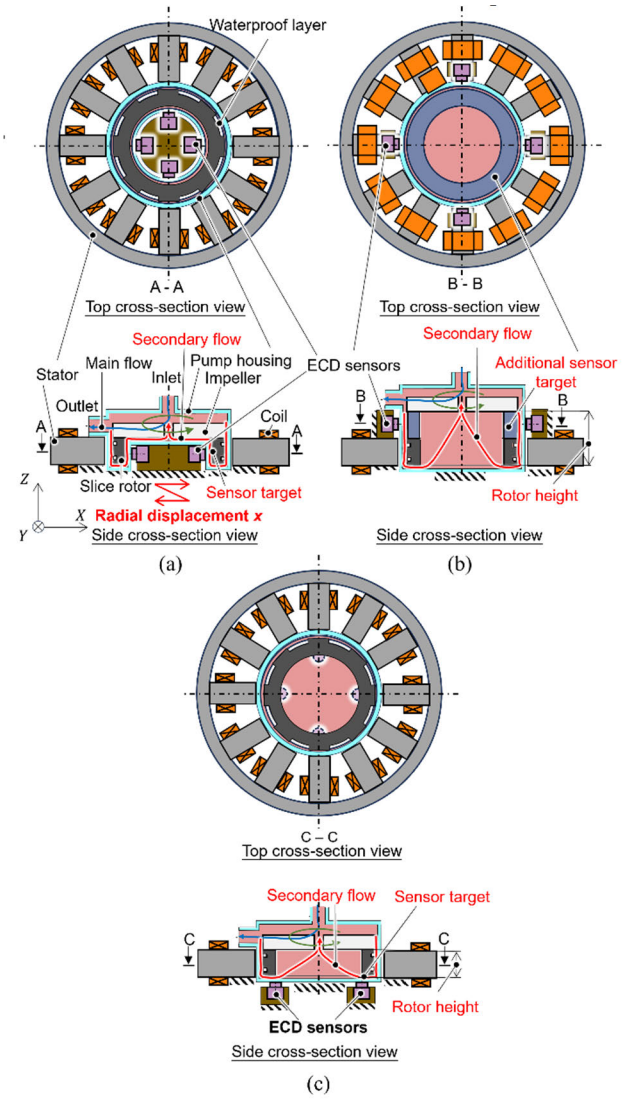

FIGURE 2. CBP utilizing a BELRSM with different sensor placements: (a) Pump head structure with the sensor placement inside the slice rotor; (b) Pump head structure with the sensor placement outside the slice rotor; (c) Pump head structure with the proposed sensor placement under the slice rotor.

in the radial direction. Conventional methods, such as the placement of the sensor target on the inner circumference of the slice rotor or the use of an additional cylindrical sensor target on the upper or lower part of the slice rotor, have limited CBP performance improvements due to the limitation of the pump head structure, as shown in Figs. 2 (a) and (b). Placing ECD sensors on the inner side of the slice rotor, as shown in Fig. 2 (a), renders the flow path in the pump head complex, resulting in the narrowing of the secondary flow and an increase in fluid resistance, subsequently leading to more hemolysis and thrombus formation in the CBP [18], [19]. Moreover, placing ECD sensors outside, constrained by the limited stator space, necessitates an increase in the height of the rotor to acquire additional sensor targets, as shown in Fig. 2 (b), leading to a rise in the initial priming volume of the pump head. A pump head with a larger initial fill volume results in increased blood product usage and an enlarged contact area between blood and the pump housing surface, leading to hemodilution and an elevated risk of complications during transfusion. Some sensorless radial methods, such as the observer-based calculation method [20], [21] and PWM injection method [22], [23], have been proposed for use with no sensor targets to solve this problem. However, the measurement accuracy and bandwidth of these methods cannot meet the requirements.

This study aims to increase the design freedom of the CBP using the BELRSM by moving the ECD sensors from their conventional placement on the side of the rotor, as shown in Figs. 2 (a) and (b), to the underside of the rotor, as shown in Fig. 2 (c), while maintaining the same radial displacement measurement accuracy. Therefore, a radial displacement measurement method for the BELRSM rotor is proposed by placing the ECD sensors under the rotor. In the proposed sensor placement, the bottom surface is used as the sensor target, which is independent of the rotor angle. Compared with the conventional placement method, this placement can avoid an increase in the initial filling volume of the disposable head by eliminating the additional sensor target. Moreover, this placement avoids occupying the inner space of the rotor.

We conducted a preliminary experiment to test the characteristics of the ECD sensor under the rotor to explore the feasibility of radial displacement measurement using the proposed placement. However, ECD sensors at that location make obtaining highly accurate radial displacement challenging due to interference from multiple-DOF displacement and nonlinear effects on the ECD sensor output. Therefore, we propose seven ECD sensor placements to compensate for the axial and tilt movement effects and propose some methods to establish the relationship between radial displacement and the output voltages of the seven sensors. The developed BELRSM used for CBP in the previous research [3] is utilized for the experiment. We tentatively propose a polynomial fitting method to establish this relationship. However, this method results in unacceptable measurement errors owing to sensor calibration and assumption inaccuracies. We propose using a neural network (NN) method to establish this nonlinear and interfering relationship automatically to improve measurement accuracy, which is implemented in displacement feedback control and successfully achieves magnetic suspension.

The remainder of this paper is organized as follows. The measurement principle of the proposed method is introduced in Section II, including radial displacement measurement using ECD sensors under the rotor, a preliminary experiment, and a seven-sensor placement. In Section III, the CBP utilizing the previously developed BELRSM is introduced. In Section IV, displacement estimation based on the polynomial fitting method is examined. In Section V, displacement estimation using the NN method is explained to improve the measurement accuracy and overcome sensor calibration difficulties. The experimental method and results utilizing

the NN method are presented in Section VI, comprising the experimental method, sensor measurement characteristics, and displacement feedback experimental results. A discussion on the size of the dataset for NN training, number of sensors, and dataset capture in the commercial application for NN training is presented in Section VII. Finally, conclusions are presented in Section VIII.

II. MEASUREMENT PRINCIPLE

A. RADIAL DISPLACEMENT MEASUREMENT USING ECD SENSORS UNDER THE ROTOR

We propose the placement of ECD sensors under the inner edge of the bottom of the rotor. This placement addresses the challenge of radial displacement measurement in the saliency slice rotor of the BELRSM using ECD sensors without mounting an additional sensor target or placing the sensors inside the rotor, as shown in Fig. 2 (c). However, the output voltage of the ECD sensor is influenced by the axial and tilt motions of the rotor, rendering the direct derivation of the radial displacement from the sensor output voltage challenging.

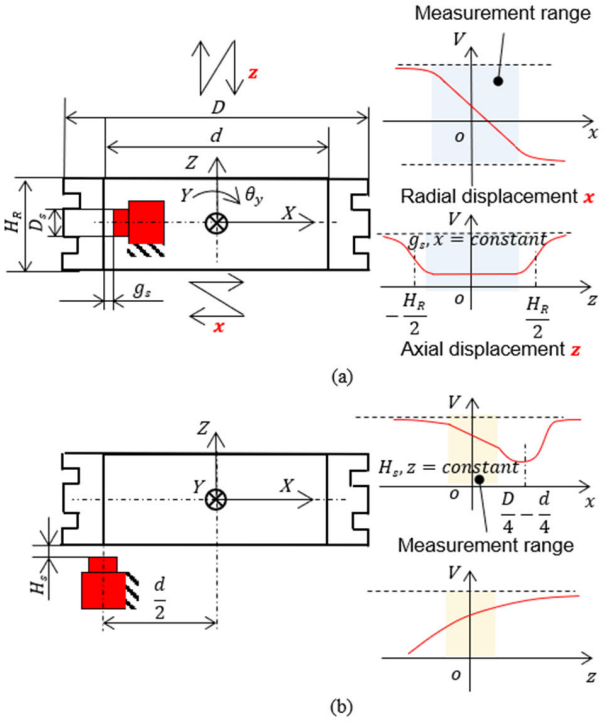

FIGURE 3. Output voltages from the ECD sensor in response to rotor displacements with different sensor placements: (a) Conventional sensor placement; (b) Proposed sensor placement.

Fig. 3 qualitatively shows the variation of output voltages of ECD sensors with rotor displacement under conventional and proposed sensor placements. The conventional placement of the ECD sensor for radial displacement measurement is shown in Fig. 3 (a). The output voltage of the ECD sensor exhibits a linear correlation with the radial displacement x within a specific range and eventually reaches saturation. Suppose the height of the rotor H_R is sufficiently larger compared with the diameter of the sensor probe D_s. In that case, given constant initial radial installation distance g_s and radial displacement x, the output voltages of the ECD sensor are not influenced by the axial displacement z when the probe is not too close to the upper and lower ends.

In contrast, the proposed placement of the ECD sensor at the inner edge of the slice rotor bottom is shown in Fig. 3 (b). The centerline of the sensor probe is *d/2* away from the centerline of the rotor in the radial direction. The placement results in a linear variation in the output voltage of the ECD sensor within a small radial displacement x when the initial axial installation distance H_s and axial displacement z remain constant. However, the axial displacement z also influences the output voltage because the sensor target (rotor bottom surface) directly faces the sensor probe. Therefore, the influence of the axial and tilt motions on the output voltage should be considered when accurately measuring the radial displacement.

B. PRELIMINARY EXPERIMENT

A preliminary experiment was conducted to validate the feasibility of the proposed sensor placement method to quantitatively verify the relationship between the output voltage of the ECD sensor and the three individual DOF movements under the proposed sensor placement. The dimensions of the slice rotor were the same as those of a BELRSM [3] for disposable CBP. The bottom rotor shape was a flat ring and the inner diameter d and outer diameter D of the slice rotor were 38 and 50 mm, respectively. The thickness of the rotor and rotor teeth was 13.4 mm and 7.8 mm, respectively. The ECD sensor (PU-05, AEC Corp, Japan) was chosen, which features a probe diameter of 5 mm and generates output voltages ranging from 0 to 2 mm within a linear output of ±5 V. The sensitivity of the ECD sensor is 5 V/mm within the standard measurement range.

The ECD sensor was placed parallel to the X-axis at an initial axial installation distance H_s of 2.1 mm from the bottom surface, like Fig. 3 (b). This initial axial distance H_s is determined by assuming the thickness of the bottom housing, waterproof layer, and fluid gap in the actual CBP, which exceeds the standard linear measurement range. The initial radial distance between the centerlines of the sensor probe and rotor was half d (19 mm). Two microstages were used to change the axial and radial positions of the sensor probe and tilt angle of the rotor from the initial position and attitude, respectively. We measured the sensor output voltages for each DOF of the rotor motion. With the proposed sensor placement, the tilt angle θ_x around the X-axis and the radial displacement y negligibly influenced the output voltages. The tilt angle θ_y around the Y-axis, the axial displacement z, and the radial displacement x were considered.

Fig. 4 presents the measurement results of the preliminary experiment, depicting the relationships between the output voltages of the ECD sensor and three individual DOF

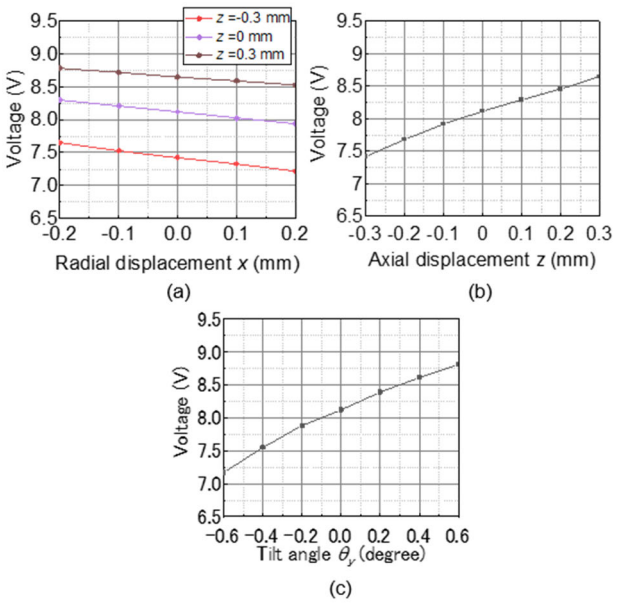

FIGURE 4. Relationships between the output voltages of the ECD sensor and three individual DOF movements by preliminary experiment: (a) Radial displacement from different axial displacements; (b) Axial displacement from the initial position; (c) Tilt angle from the initial attitude.

movements, beginning from the initial position and attitude. The output voltage of the sensor was coupled with these three-DOF movements. As shown in Fig. 4 (a), when the axial displacement and inclination remain constant, the output voltage of the sensor exhibited a linear relationship with the radial displacement. Moreover, the slope and intercept of the linear relationship were influenced by axial displacement. The radial displacement was derived from the output voltage of the sensors by considering the axial displacement and tilt angle. Figs. 4 (b) and 4 (c) illustrate that the sensor output is susceptible to interference from axial and tilting movements, resulting in significant voltage changes. Consequently, compensation for these interferences is essential.

C. SEVEN ECD SENSOR PLACEMENT

To compensate for the effect of the axial and tilt motions, seven ECD sensors placed below the rotor, as shown in Fig. 5 (a), were proposed to calculate the axial displacement, tilt angle, and radial displacement. Three ECD sensors S_i (i = 1-3) located at the center of the circular ring of the bottom of the rotor were used to calculate the axial displacement and tilt angles, as shown in Fig. 5 (b). The effects of the radial motion on the output voltages were negligible because of the central placement of the sensors S_i. The output voltages of the sensors can be assumed as shown in (1):

$$V_i = \mathrm{V_i}(z, \theta_x, \theta_y) \tag{1}$$

where V_i denotes the output voltage of each sensor S_i. z is the axial displacement. θ_x and θ_y are the tilt angles around the X- and Y- axes, respectively.

The other four ECD sensors, S_j (j = 4-7), were installed under the inner edge of the rotor bottom parallel to the X- and Y-axes, as shown in Fig. 5 (b). Each pair of S_6 and S_7, S_4, and S_5 was used to differentially measure the radial displacements in the X- and Y-directions from the output voltage V_j to improve the measurement accuracy. Because the sensors were placed parallel to the coordinate axes, each output voltage of the sensor could be assumed to be related to the motion of the three DOFs, as shown in (2)-(5):

$$V_4 = \mathrm{V_4}(y, z, \theta_x) \tag{2}$$
$$V_5 = \mathrm{V_5}(y, z, \theta_x) \tag{3}$$
$$V_6 = \mathrm{V_6}(x, z, \theta_y) \tag{4}$$
$$V_7 = \mathrm{V_7}(x, z, \theta_y) \tag{5}$$

where x and y denote the radial displacements in the X- and Y-directions, respectively. Assuming these functions can be established through sensor calibration, the output of seven ECD sensors can then be utilized to deduce the radial displacement in both the X- and Y-directions.

In theory, all five DOFs (radial, axial, and tilt motions) affect the output voltage of the ECD sensor placed under the rotor. To achieve decoupling, a minimum number of five sensors is required to derive radial displacement from the output voltages of the ECD sensors. To further compensate for nonlinearity, reduce temperature drift and noise, and enhance sensitivity, we use seven ECD sensors with differential placement along the X and Y axes. The configuration of five-sensor placement was discussed in Section VII-B.

III. EXPERIMENT SETUP OF BELRSM

A. BELRSM STRUCTURE

To establish the relationship between the multiple-DOF motion of the rotor and the output voltage of each sensor and to conduct the magnetic suspension experiments using the proposed method, we utilized a previously developed CBP utilizing the proposed BELRSM [3]. Fig. 6 shows the configuration of the mechanical structure of the CBP utilizing BELRSM with two sensor systems for sensor calibration, respectively. The proposed ECD sensor system used the same model PU-05 as the previous preliminary experiment, and the radial ECD sensor system used a special model PU-05-122-XYZ with a shorter probe case length.

The BELRSM incorporated twelve stator teeth on the stator and eight teeth on the periphery of the rotor. Besides, it featured two vertical-magnetized permanent-magnet (PM) rings and two iron rings symmetrically placed above and below the tips of the stator teeth to provide the flux bias. The current flowing through each combined winding, wound around every stator tooth, comprised rotation and suspension currents. These windings were connected with twelve linear amplifiers and windings grouped into four categories. Among these groups, the two opposing groups controlled radial magnetic suspension in one direction by varying the magnetic flux density in the air gap between the rotor and stator. This variation was achieved through the superposition of the suspension

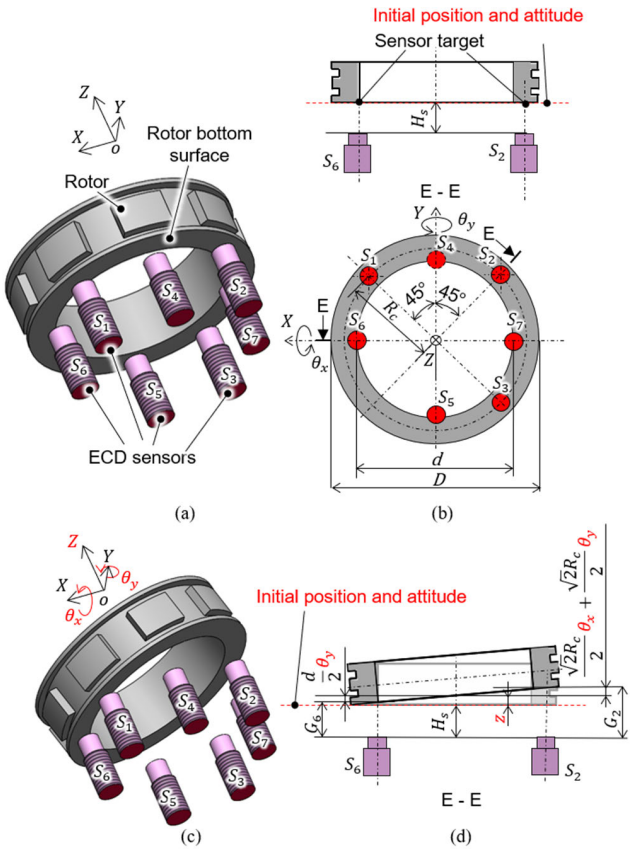

FIGURE 5. Seven ECD sensor placement: (a) Schematic diagram of the seven ECD sensor placement with initial position and attitude; (b) Bottom and side cross-section view of the seven ECD sensor placement with initial position and attitude; (c) Schematic diagram of the seven ECD sensor placement with rotor displacements z, θ_y, and θ_x; (d) Side cross-section view of the seven ECD sensor placement with rotor displacements z, θ_y, and θ_x.

flux generated by the current and the flux bias created by the PM rings. Within these four groups, there were three phases: U, V, and W. By sequentially energizing U, V, and W, the rotor can be rotated continuously. The outer diameter and height of the BELRSM measured 144 mm and 32.4 mm, respectively. The disposable pump head was vertically inserted into the BELRSM stator, and the gravitational force acting on the rotor in the axial direction was passively supported by the flux bias generated by the PM rings.

B. SENSOR SYSTEM OF THE BELRSM

The schematic diagram of the sensor placement in BELRSM for sensor calibration and magnetic suspension experiment is shown in Fig. 6, consisting of ECD sensors positioned below the rotor and on the inner side of the rotor. The BELRSM previously achieved the radial displacement feedback control utilizing the radial ECD sensors on the inner side of the rotor [3], which served as a reference in this research. The carrier frequencies of the ECD amplifiers were selected carefully to avoid interference between the ECD sensor probes. The radial ECD sensors are individually calibrated to obtain radial displacement, as mentioned in previous research [3].

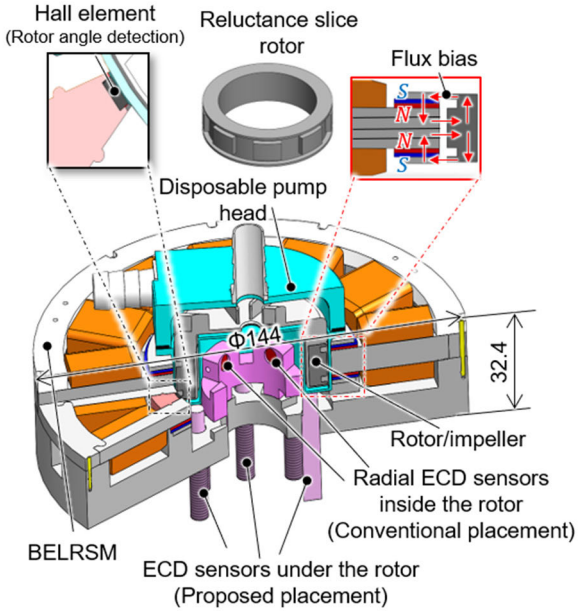

FIGURE 6. Configuration of the mechanical structure of the CBP utilizing BELRSM with two sensor systems.

However, for the proposed seven-sensor system, calibration needs to account for the influence of multiple rotor motions. In the following two chapters, the sensor calibration methods will be proposed and verified.

IV. DISPLACEMENT MEASUREMENT BASED ON THE POLYNOMIAL FITTING METHOD

A. ECD SENSOR CALIBRATION METHODS USING THE POLYNOMIAL FITTING METHOD

1) AXIAL DISPLACEMENT AND TILT ANGLES CALCULATION

Since the ECD sensors S_i ($i = 1$-3) are placed in the middle of the rotor bottom, the influence of minor radial displacement (x, y) on the measured sensor output V_i can be ignored. z, θ_x, and θ_y can be derived from the output voltage V_i of S_i. Through each sensor calibration, the measured V_i can be used to identify each axial distance G_i by each polynomial function u_i using (6):

$$G_i = \mathrm{u_i}(V_i)$$
$$\mathrm{u_i}\,(V_i) = \sum_{l=0}^{q} \alpha_{il}(V_i)^l \tag{6}$$

where G_i is defined as the axial distances between the sensor target (the bottom surface of the rotor) and sensor probes' center points of S_i. The definitions of G_i simplify the relationship between the multiple DOF motions of the rotor. q is the order of the polynomial ($q = 0, 1, 2, \ldots$) and α_{il} is the coefficient of each polynomial term for each $\mathrm{u_i}$.

G_i of each ECD sensor is decided by the sensor installation position and rotor axial and tilt motions, including z, θ_x, and θ_y. Fig. 5 (c) shows the schematic diagram of the seven ECD sensor placement with rotor displacements z, θ_y, and θ_x. Fig. 5 (d) shows the geometrical relationships among axial distance G_2, axial displacement z, tilt angles θ_x and θ_y, and initial installation distance H_s as examples. After obtaining

the G_i, these geometrical relationships of each sensor probe S_i can be assumed as in (7) based on (1) when $(x, y) = (0, 0)$:

$$\begin{bmatrix} G_1 \\ G_2 \\ G_3 \end{bmatrix} = \begin{bmatrix} 1 & \frac{\sqrt{2}}{2}R_c & -\frac{\sqrt{2}}{2}R_c \\ 1 & \frac{\sqrt{2}}{2}R_c & \frac{\sqrt{2}}{2}R_c \\ 1 & -\frac{\sqrt{2}}{2}R_c & \frac{\sqrt{2}}{2}R_c \end{bmatrix} \begin{bmatrix} z \\ \theta_x \\ \theta_y \end{bmatrix} + \begin{bmatrix} 1 \\ 1 \\ 1 \end{bmatrix} H_s \quad (7)$$

where R_c is the radial distance between the centerlines of the sensor probes S_i and rotor. Because the θ_x and θ_y are sufficiently small, tan θ_x and tan θ_y are approximately equal to θ_x and θ_y, respectively. z, θ_x, and θ_y can be derived from G_i and H_s using (8):

$$\begin{bmatrix} z \\ \theta_x \\ \theta_y \end{bmatrix} = \begin{bmatrix} 1/2 & 0 & 1/2 \\ 0 & \frac{\sqrt{2}}{2R_c} & -\frac{\sqrt{2}}{2R_c} \\ -\frac{\sqrt{2}}{2R_c} & \frac{\sqrt{2}}{2R_c} & 0 \end{bmatrix} \begin{bmatrix} G_1 - H_s \\ G_2 - H_s \\ G_3 - H_s \end{bmatrix} \quad (8)$$

Therefore, since a small radial displacement will not affect the output change of S_i, the z, θ_x, and θ_y can be derived from the measured V_i, polynomial function $\mathrm{u_i}$ of V_i obtained by sensor calibration, initial installation distance H_s, and (8).

2) RADIAL DISPLACEMENT CALCULATION

The output voltage V_j of four ECD sensors S_j (j = 4-7) can be used to calculate the radial displacements in the X- and Y-directions after obtaining z, θ_x, and θ_y. As shown in Fig. 4 (a), the output voltages of the sensors S_j exhibit a linear relationship with the radial displacement when the motions of the other DOFs remained constant. These relationships of each S_j can be fitted with a first-order linear equation in the X- and Y-directions using (9)-(12):

$$V_4 = k_4(G_4)\, y + b_4(G_4) \quad (9)$$
$$V_5 = k_5(G_5)\, y + b_5(G_5) \quad (10)$$
$$V_6 = k_6(G_6)\, x + b_6(G_6) \quad (11)$$
$$V_7 = k_7(G_7)\, x + b_7(G_7) \quad (12)$$

where $\mathrm{k_j}(G_j)$ and $\mathrm{b_j}(G_j)$ (j = 4-7) represent the slope and intercept of the linear equation, respectively. We assume that the slope and intercept of the first-order function are only associated with the axial distance G_j of S_j.

Supposing $(x, y) = (0, 0)$, G_j is defined as the axial distances between the sensor target and sensor probes' center points of S_j. G_6 is shown as an example in Fig. 5 (d). When z, θ_x, and θ_y are obtained, G_j can be calculated through the geometrical relationships using (13):

$$\begin{bmatrix} G_4 \\ G_5 \\ G_6 \\ G_7 \end{bmatrix} = \begin{bmatrix} 1 & d/2 & 0 \\ 1 & -d/2 & 0 \\ 1 & 0 & -d/2 \\ 1 & 0 & d/2 \end{bmatrix} \begin{bmatrix} z \\ \theta_x \\ \theta_y \end{bmatrix} + \begin{bmatrix} 1 \\ 1 \\ 1 \\ 1 \end{bmatrix} H_s \quad (13)$$

$\mathrm{k_j}$ and $\mathrm{b_j}$ can be represented by polynomial functions of G_j using (14) and (15), respectively.

$$\mathrm{k_j}\left(G_j\right) = \sum_{l=0}^{q} \beta_{jl} (G_j)^l \quad (14)$$
$$\mathrm{b_j}\left(G_j\right) = \sum_{l=0}^{q} \gamma_{jl} (G_j)^l \quad (15)$$

where β_{jl} and γ_{jl} are the coefficients of each polynomial term $\mathrm{k_j}$ and $\mathrm{b_j}$, respectively. The coefficients β_{jl} and γ_{jl} can be obtained by altering the G_j, recording the various $\mathrm{k_j}$ and $\mathrm{b_j}$, and subsequently employing a polynomial for curve fitting. After determining these coefficients, we can initially calculate the value of $\mathrm{k_j}(G_j)$ and $\mathrm{b_j}(G_j)$ by substituting calculated from (13) into (14) and (15) and subsequently deduce the radial displacements in the X- and Y-directions using (9)-(12) and measured output voltages V_j of S_j.

To increase the measurement accuracy and suppress the signal noise and temperature drift, the radial displacements in the X- and Y- directions were derived using a pair of ECD sensors between S_6 and S_7, and S_4 and S_5, respectively. By subtracting (12) from (11) and (10) from (9), the differential measurements can be expressed as (16) and (17):

$$x = \frac{V_6 - V_7 + b_7(G_7) - b_6(G_6)}{k_6(G_6) - k_7(G_7)} \quad (16)$$
$$y = \frac{V_4 - V_5 + b_5(G_5) - b_4(G_4)}{k_4(G_4) - k_5(G_5)} \quad (17)$$

B. EXPERIMENTAL METHOD AND RESULTS OF THE POLYNOMIAL FITTING METHOD

G_i and G_j were experimentally changed to identify the polynomial function order and coefficients of $\mathrm{u_i}$, $\mathrm{k_j}$, and $\mathrm{b_j}$. Fig. 6 shows the experimental setup with two sensor systems for sensor calibration. In the polynomial fitting method, the top housing was removed and the rotor was directly placed into the bottom housing and pressed with a pressure plate to prevent tilting. To alter the radial displacement (x, y) of the rotor and the axial distances G_i and G_j, several polyester films of 0.1 mm thick were inserted into the radial and axial gaps of the rotor, respectively. The output voltages of S_i and S_j and the radial displacement (x, y) of the rotor were measured at different positions for sensor calibration. Fig. 7 shows the experimental sensor calibration results using the polynomial fitting method.

The G_i at different output voltage V_i and the 2nd-order fitted curves of these relationships are shown in Fig. 7 (a), whereas the variation of V_4 with y at different G_4 values and the fitted line of S_4 are shown in Fig 7. (b). The two pairs of ECD sensors, S_6 and S_7, S_4 and S_5, have similar linear trends with radial displacements in the X- and Y-directions, respectively. The slopes and intercepts of the fitted linear equations of S_j with different G_j are shown in Figs. 7 (c) and (d), respectively. These relationships were fitted using a 2nd -order polynomial in the figure.

After implementing the relationships between V_i and G_i along with V_j and G_j in the digital signal processor (DSP), the radial displacement can be measured from the output voltages of the seven ECD sensors (proposed sensor system). The measurement results were compared with the outputs of the radial ECD sensors to evaluate the measurement accuracy. The BELRSM rotor was not magnetically levitated but only moved around the wall of the bottom housing by injecting the sinusoidal current into the coil. The radial displacement

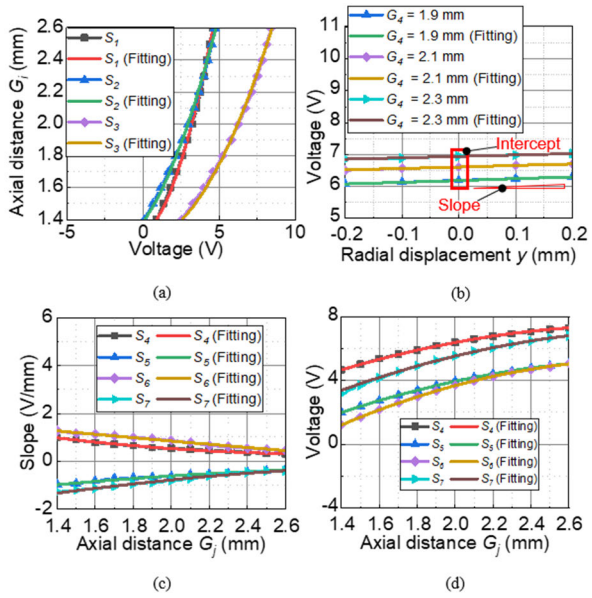

FIGURE 7. Experimental sensor calibration results using the polynomial fitting method: (a) Axial distance G_i at different output voltages V_i and 2nd-order fitted curves; (b) Variation of output voltage V_4 with radial displacement y at different axial distances G_4 and the fitted lines of S_4; (c) Slopes of the linear equations of S_j with different axial distances G_j; (d) Intercepts of the linear equations of S_j with different axial distances G_j.

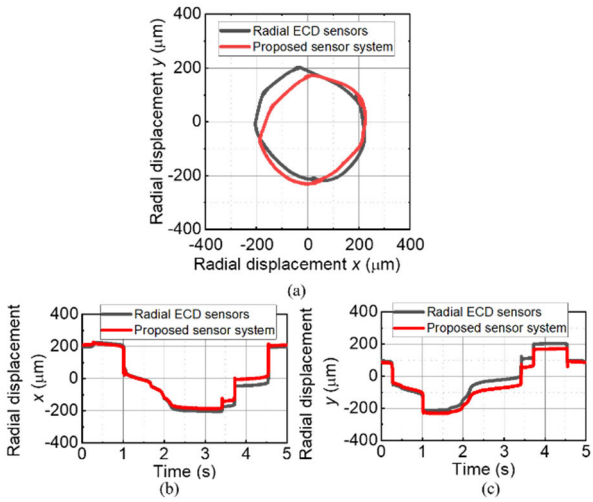

FIGURE 8. Experimental results of the displacement estimation based on the polynomial fitting method: (a) Trajectory of radial motion (x, y); (b) Radial displacement x; (c) Radial displacement y.

of the rotor was measured using the radial ECD sensors and the proposed sensor system, respectively, as shown in Fig. 8. The maximum error between the proposed sensor system and radial ECD sensors was 44 μm and 56 μm in X- and Y- directions, respectively, which is unacceptable for the displacement feedback control system for magnetic suspension.

Calibration of the ECD sensors should be performed in the BELRSM to ensure accuracy and repeatability. The large measurement errors with the polynomial fitting method resulted from the inaccuracy of the sensor calibration and calculated intercept $b_j(G_j)$. Polyester films of 0.1 mm thick could not provide a sufficiently small radial displacement variation in the 0.2 mm radial gap for sensor calibration. In addition, because of the sensor placement at the inner edge of the bottom of the rotor, the assumption that G_j is used to ignore the influence of rotor inclination had an error in the intercept calculation, which can influence the radial displacement measurement. Sensor calibration using the NN method is proposed in the next section to establish complex nonlinear relationships and achieve accurate measurement of rotor displacement.

V. DISPLACEMENT MEASUREMENT BASED ON THE NN METHOD

A. ECD SENSOR CALIBRATION METHOD USING THE NN METHOD

The relationship between the seven ECD sensor outputs and two radially mounted ECD sensors fitted with higher-order polynomial functions was clarified. However, a relationship with sufficient accuracy has not been obtained. A feedforward NN based on a backpropagation algorithm was used to resolve the problem of inaccuracy because it can model nonlinear input-output relationships and the backpropagation algorithm can automatically determine the NN parameters.

The NN architecture in Fig. 9 includes the input, hidden, and output layers. The backend calculation of the NN mainly includes model inference and training process. In model inference, input data undergoes a forward pass through the NN, with each layer applying learned weights and activation functions to generate predicted results.

Each layer comprises several neuron units that receive inputs from all neurons in the preceding layer. The total input was calculated as the sum of the neuron outputs in the preceding layer multiplied by the weights and added to the bias. Subsequently, this input was transformed using an activation function to produce the output of the neuron. The forward propagation equation and activation function are as shown in (18) and (19):

$$N_n = \sum_{m=1}^{p} w_{nm} a_m + B_n (n = 1, 2, \ldots, c) \tag{18}$$

$$a_n = \mathrm{g}(N_n) = \frac{2}{1 + e^{-2N_n}} - 1 \tag{19}$$

where p and c are the numbers of neurons in the preceding and current layers, respectively. N_n is the total input of the nth neuron in the current layer from the preceding layer. w_{nm} and B_n are the weight of the connection from the mth neuron in the preceding layer to the nth neuron in the current layer and the bias values of the nth neuron in the current layer, respectively. a_n and a_m are the nth and mth neuron outputs in the current and preceding layers, respectively. g is the appropriate activation function that uses a hyperbolic tangential sigmoid function.

The training process is backpropagation, which computes gradients of the loss for model parameters, such as weights

and biases, facilitating the optimization of weights through algorithms. The computation of the weights and biases in an NN requires a dataset for NN training comprising the input and corresponding desired output data. The weights were randomly assigned suitable initial values and iteratively updated using the gradient descent method to minimize the mean square errors (MSEs) between the predicted and desired output data. The MSEs were calculated as the average of the squared difference between the predicted and desired outputs over the entire dataset for NN training as the loss function. The backpropagation algorithm was used to propagate the error back through the NN, as shown in (20)-(23) and update the weights and biases in each layer.

$$\hat{w}_{nm} = w_{nm} + \Delta w_{nm} \tag{20}$$

$$\Delta w_{nm} = -\eta \frac{\partial E}{\partial N_n} a_m \tag{21}$$

$$\hat{B}_n = B_n + \Delta B_n \tag{22}$$

$$\Delta B_n = -\eta \frac{\partial E}{\partial N_n} \tag{23}$$

where Δw_{nm} and ΔB_n are the weight and bias correction terms, respectively. $\hat{w}_{nm}$ and $\hat{B}_n$ represent the updated weights and biases, respectively. E is the MSEs and η is the learning rate parameter to control the convergence rate of the NN and stability. The training function is the Levenberg-Marquardt algorithm. This process was repeated for several epochs until the MSEs reached a minimum or converged to a certain value.

In the case of the computational time of the NN and real-time implementation in the DSP, we designed an NN with one input layer, one hidden layer, and one output layer. The hidden, input, and output layers comprise ten, seven, and two neurons, respectively. The neurons in the input layer received the output voltages of the seven ECD sensors, whereas the radial displacements measured in the X- and Y-directions by the radial ECD sensors were fed into the output layer. One hidden layer with ten neurons is adapted for establishing the relationship between sensor output voltages and radial displacements, which reaches a tradeoff among precision fitting requirements, training time, and hardware resources for real-time implementation. The NN was designed using the NN toolbox in MATLAB.

Increasing the number of neurons and hidden layers allows for the establishment of more complex NN models, enabling more sophisticated nonlinear fitting and potentially enhancing the accuracy of the fitting process. However, it is important to be cautious about using an excessive number of neurons and hidden layers, as it can lead to overfitting, where the model becomes overly specific to the training data and performs poorly on unseen data. Besides, complex models entail a greater number of parameters, leading to increased training times and higher utilization of hardware resources for real-time implementation.

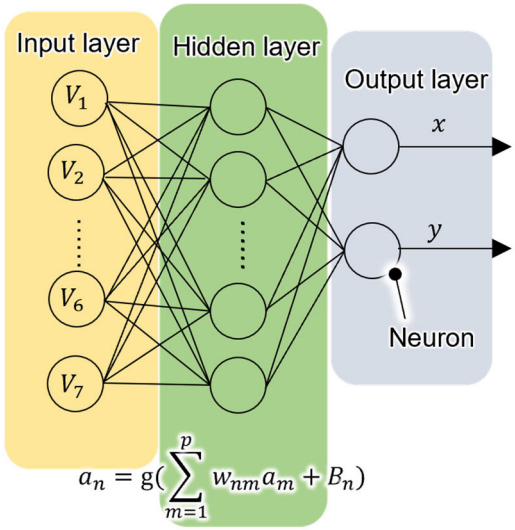

FIGURE 9. Neural network architecture.

B. CONSTRUCTION OF THE DATASET FOR NN TRAINING

Collecting the time response points of the measured output voltage of the proposed ECD sensor system and the measured radial displacement using the radial ECD sensor system under different experimental conditions are used to establish a dataset for NN training. To design a precise NN, a dataset for NN training encompassing various wide-range positions and attitudes of the slice rotor is required. An outlet-clamped mock circulatory loop filled with 40 wt% glycerol aqueous solution was used, as previously described [3]. The rotor of the BELRSM was magnetically suspended using the radial displacements measured by the radial ECD sensors, as mentioned in Section III-B. The axial displacement and tilt angles were measured using three calibrated ECD sensors S_i, as described in Section IV. A. The radial positioning and speed feedback control systems were consistent with those used in previous studies [3]. The controller parameters are listed in Tables 1 and 2, respectively.

TABLE 1. Displacement feedback control parameters.

Parameters	Values
Proportional gain [A/m]	5000
Integral gain [A/m·s]	8000
Derivative gain [A·s /m]	4
Cut-off frequency of the first-order LPF for derivative part [Hz]	500
Cut-off frequency of the second-order LPF [Hz]	200
Damping ratio of the second-order LPF	0.707

TABLE 2. Speed feedback control parameters.

Parameters	Values
Proportional gain [A/rpm]	0.005
Integral gain [A/rpm·s]	0.001

TABLE 3. Lists of the experimental condition types of the dataset for NN training.

Experimental condition types of the dataset for NN training		
Types	Parameters	Positions and values
Magnetic suspension startup with different initial positions	Initial positions	Positive and negative directions of the X-axis; Positive and negative directions of the Y-axis
Magnetic suspension with the different radial circular orbit targets	Amplitudes of several radial circular orbit targets [μm]	0/10/20/30/40/50 60/70/80/90/100
Magnetic suspension at different rotational speeds with the different radial circular orbit targets	Amplitudes of several radial circular orbit targets [μm]	0/10/20/30
	Rotational speeds [rpm]	100/300/500/700/900 1100/1300/1500/1700

Different experimental conditions were set to simulate various rotor positions and attitudes. The startup responses with varying initial positions were measured. Furthermore, radial circular orbital motion with various amplitudes under non-rotating and rotating conditions was measured. The types of experimental conditions for the dataset for NN training are listed in Table 3.

The measured radial, axial, and tilt responses during the magnetic suspension startup from different initial positions in the positive and negative directions of the X- and Y-axes with the same PID controller parameters in the suspension control system are shown in Fig. 10. The radial orbits differ because of their different initial positions. The axial and tilt orbits also exhibit variations with different initial values.

The measured radial, axial, and tilt responses when several radial circular orbit targets with amplitudes of 20, 40, 60, and 80 μm at a frequency of 1 Hz were input into the compensator during non-rotation are shown in Fig. 11. Different radial circular orbits are shown in Fig. 11 (a). Larger amplitudes of the radial circular orbit resulted in larger

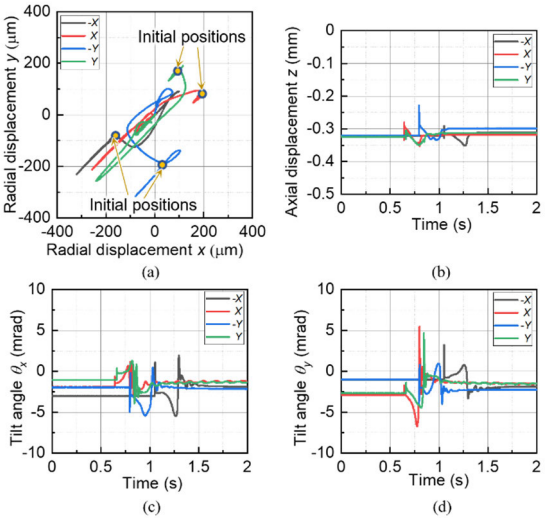

FIGURE 10. Magnetic suspension startup with different initial positions in the positive and negative directions of the X- and Y-axes: (a) Trajectories of rotor radial motion (x, y) measured by the radial ECD sensors; (b) Axial displacement z measured by the calibrated ECD sensors S_i; (c) Tilt angle θ_x measured by the calibrated ECD sensors S_i; (d) Tilt angle θ_y measured by the calibrated ECD sensors S_i.

variations in the axial displacements and tilt angles, as shown in Figs. 11 (b), (c), and (d), respectively.

The average axial displacements were obtained by varying the rotational speed from 300 to 1500 rpm in the outlet-clamped mock circulation loop, providing a dataset with a wider range of axial displacement variations owing to the difference in the hydraulic pressure between the upper and lower surfaces of the rotor/impeller is shown in Fig. 12.

The measured radial, axial, and tilt responses of the compensator at a speed of 900 rpm are shown in Fig. 13 when several small radial circular orbit targets with amplitudes of 10, 20, and 30 μm at a frequency of 1 Hz were input. The amplitudes of the axial displacement and tilt angles also vary with the amplitudes of the radial circular orbit target, as shown in Figs. 13 (b), (c), and (d). The radial, axial, and tilt responses exhibited the same trends at the other rotational speeds.

To accurately measure the radial displacement during suspension under startup, non-rotating, and rotating conditions, a diverse dataset for NN training that encompasses significant variations in the displacement and attitude of the rotor under these conditions is crucial. This was achieved by adjusting the control parameters, such as the reference displacement and rotational speed. For the suspension startup and non-rotating conditions, different startup initial positions were set to simulate the substantial variation in inclination and axial displacement resulting from the large positioning force during startup, as shown in Fig. 10. In addition, various radial circular orbits were employed to provide a wide range of radial displacement changes, as shown in Fig. 11. For suspension under rotating conditions, different rotational speeds were used to simulate a broad range of axial displacement

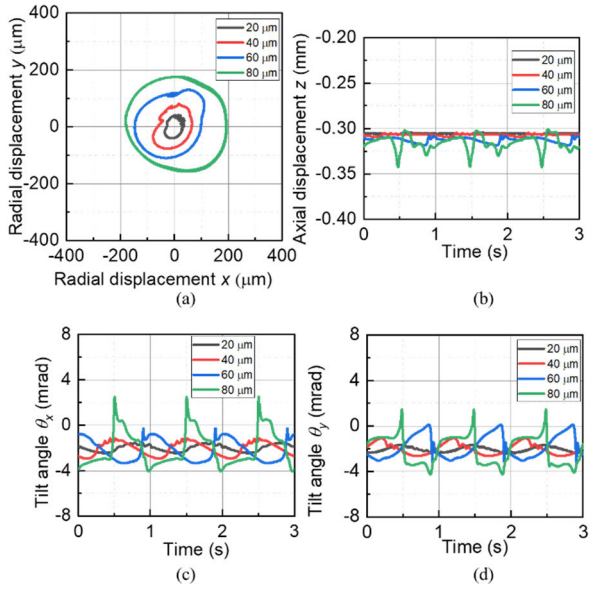

FIGURE 11. Magnetic suspension when several radial circular orbit targets with amplitudes of 20, 40, 60, and 80 μm at a frequency of 1 Hz were inputted into the compensator during non-rotation: (a) Trajectories of rotor radial motion (x, y) measured by the radial ECD sensors; (b) Axial displacement z measured by the calibrated ECD sensors S_i; (c) Tilt angle θ_x measured by the calibrated ECD sensors S_i; (d) Tilt angle θ_y measured by the calibrated ECD sensors S_i.

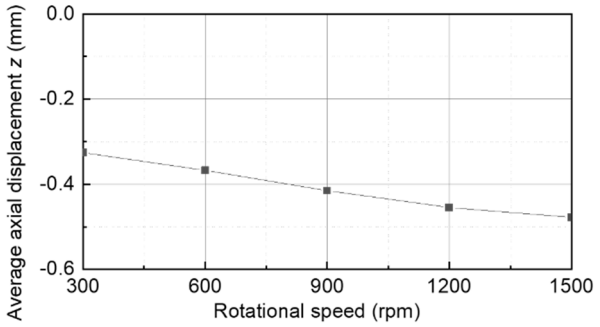

FIGURE 12. Average measured axial displacements obtained by varying the rotational speeds from 300 rpm to 1500 rpm with the outlet-clamped mock circulation loop using the calibrated ECD sensors S_i.

variations caused by the hydraulic force, as shown in Fig. 12. Furthermore, different radial circular orbits were set to simulate a large rotor inclination and radial displacement during rotation, as shown in Fig. 13.

VI. EXPERIMENTAL METHOD AND RESULTS OF THE DISPLACEMENT MEASUREMENT BASED ON THE NN METHOD

A. EXPERIMENTAL METHOD OF THE NN METHOD

The dataset used for NN training was collected for each experimental condition at a sampling frequency of 5 kHz for 3 s, as shown in Table 3. This dataset consists of a total time response point of 765000. Using the NN toolbox in MATLAB, all the time responses were randomly divided into the train, validation, and test sets in a ratio of 7: 1.5: 1.5. This results in time response points of 535500 for the train

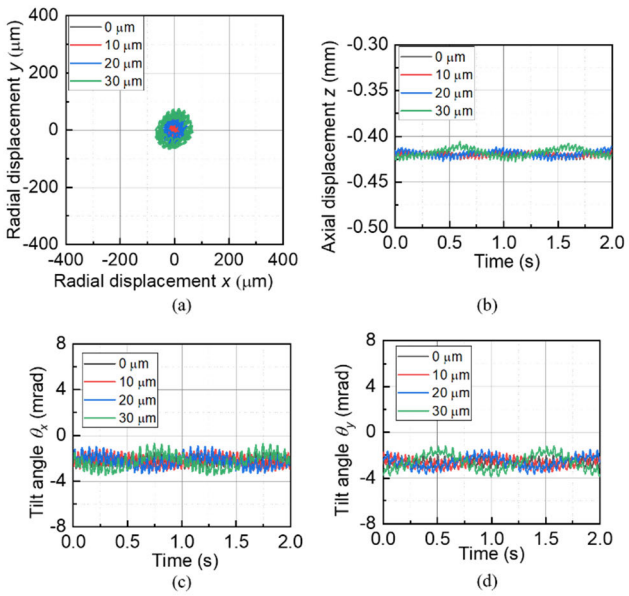

FIGURE 13. Magnetic suspension at a speed of 900 rpm when several radial circular orbit targets with amplitudes of 10, 20, and 30 μm at a frequency of 1 Hz were input into the compensator: (a) Trajectories of rotor radial motion (x, y) measured by the radial ECD sensors; (b) Axial displacement z measured by the calibrated ECD sensors S_i; (c) Tilt angle θ_x measured by the calibrated ECD sensors S_i; (d) Tilt angle θ_y measured by the calibrated ECD sensors S_i.

set, time response points of 114750 for the validation set, and time response points of 114750 for the test set, respectively. To decrease the high-frequency noise, the measured seven raw output voltages of the sensors under the rotor were passed through a 2nd-order low-pass filter (LPF) with a cut-off frequency of 200 Hz. The cut-off frequency of the LPF was identical to that used in the radial ECD sensors, as shown in Table 1.

The time responses of the measured output voltages of the seven sensors and the radial displacements measured using the radial ECD sensors under different experimental conditions were fed into the NN toolbox as the input and desired output to train the NN. The minimum MSEs of the trained NN were calculated after 1000 epochs, which was 60.3 μm^2 and the workstation (CPU: Intel® Xeon® Silver 4214R; Memory: 64GB.) used a training time of 100 min. Subsequently, the trained NN was implemented in DSP (MicroLabBox, dSPACE GmbH) to calculate the radial displacements in the X- and Y-directions from the outputs of seven sensors with a sampling frequency of 20 kHz.

We chose a sampling frequency of 5 kHz and a recording time of 3 s for each experimental condition to obtain a smaller final calculated MSEs between estimated and measured radial displacements and obtain more accurate sensor calibration. If sampling frequency and time are reduced to 500 Hz and 1 s, respectively, the final calculated MSEs will increase from 60.3 μm^2 to 63.8 μm^2 while the training time will significantly decrease from 100 min to 4 min. Therefore, to diversify the types of experiment conditions in the dataset for NN training for expanding the operational range, such as

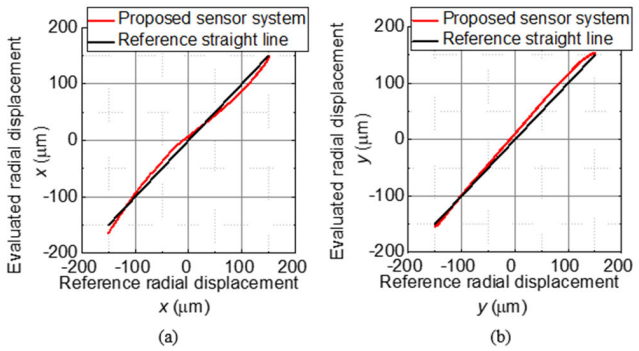

FIGURE 14. Sensor linearity between the reference radial displacement measured using radial ECD sensors and evaluated radial displacement measured using the proposed sensor system based on the NN method: (a) X direction; (b) Y direction.

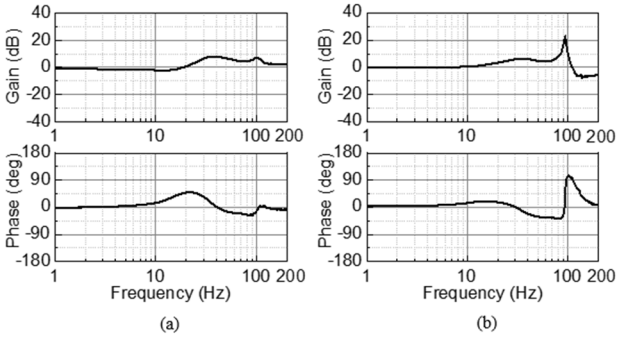

FIGURE 15. Measured frequency responses from the radial displacement measured using the radial ECD sensors system to the evaluated radial displacement measured using the proposed sensor system based on the NN method: (a) X direction; (b) Y direction.

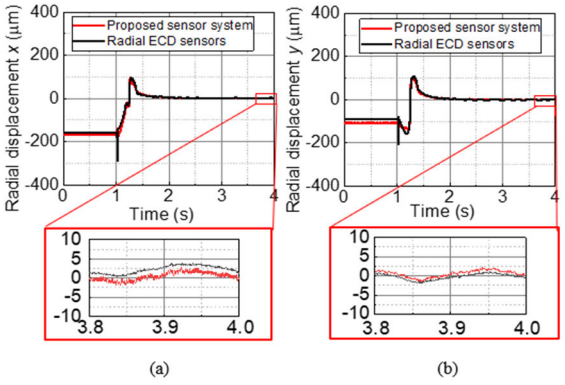

FIGURE 16. Displacement feedback control based on the evaluated radial displacement using the proposed sensor system during magnetic suspension startup: (a) X direction; (b) Y direction.

increasing the rotational speed range, we can significantly reduce training time by decreasing the sampling frequency and sampling time while maintaining fitting accuracy.

B. SENSOR MEASUREMENT CHARACTERISTICS USING THE NN METHOD

The linearity and bandwidth of the radial displacement measured using the NN were evaluated. To evaluate the linearity, the rotor of BELRSM was positioned using the radial ECD sensors, and a sinusoidal signal with a frequency of 0.1 Hz along with an amplitude of 150 μm was injected into the radial reference displacements in the X- and Y-directions. Within the range of $\pm$150 μm, the maximum errors between the evaluated radial displacement measured using the proposed sensor system and reference radial displacement measured using the radial ECD sensors were 13.6 μm and 17.1 μm in the X- and Y-directions, as shown in Figs. 14 (a) and (b), respectively.

To evaluate the measurement bandwidth, a sinusoidal current with an amplitude of 0.1 A was injected into the reference current in the X- and Y- directions. The frequency responses from the radial displacement measured using the radial ECD sensors to the evaluated radial displacement measured by the proposed sensor system using an NN method were measured. The measured frequency responses in the X- and Y-directions are shown in Figs. 15 (a) and (b), respectively, indicating that the measured bandwidth has no attenuation within the cut-off frequency of the LPF. However, certain frequency ranges exist with the measured gain greater than 0 dB. This can be attributed to the significant vibrations in the radial, axial, and tilt directions induced by the current excitation in these frequency ranges. Such large rotor motions and attitudes were not included in the previous dataset for NN training. The existing NN cannot accurately measure radial displacement within this frequency range, resulting in measurement errors.

C. DISPLACEMENT FEEDBACK EXPERIMENTAL RESULTS USING THE NN METHOD

The feedback of the radial displacements measured using the NN method achieved the startup of the magnetic suspension and stable rotation from 100 to 1700 rpm. The measured radial displacements in the X- and Y-directions during magnetic suspension startup are shown in Figs. 16 (a) and (b), respectively. The difference between the outputs of the radial ECD and proposed method was insignificant at startup. The errors during the stable condition were 3.5 and 1.5 μm in the X- and Y-directions, respectively. The measured radial displacements in the X- and Y-directions at a speed of 1700 rpm are shown in Figs. 17 (a) and (b), respectively. This is the maximum rotational speed under the experimental conditions of the previous dataset for NN training from Table 3. The root means square errors (RMSEs) between the radial displacement measured using the radial ECD sensors and that evaluated using the proposed sensor system were 11.3 and 8.8 μm in the X- and Y-directions, respectively. As shown in Table 4, the RMSEs were within 16 μm at different rotational speeds.

As the existing technique, the radial sensor system was used as a reference benchmark in the experiments to evaluate the proposed method. Compared with the existing technique using radial sensor systems, the proposed method exhibits slightly lower measurement accuracy while maintaining the same measurement bandwidth. Nevertheless, it still successfully achieves displacement feedback control during both

TABLE 4. Rmses between the radial displacements measured using the radial ECD sensors and proposed sensor system at different rotational speeds in the X- and Y- directions.

Rotational speeds [rpm]	RMSE [μm]	
	X direction	Y direction
300	12.4	16.0
600	12.6	12.3
900	12.9	9.0
1200	15.0	10.4
1500	12.0	9.8
1700	11.3	8.8

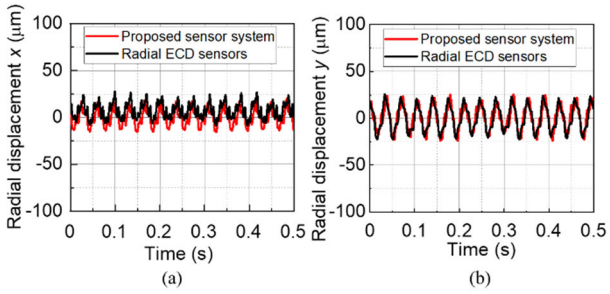

FIGURE 17. Displacement feedback control based on the evaluated radial displacement measured using the proposed sensor system at a speed of 1700 rpm: (a) X direction; (b) Y direction.

startup and rotation. Furthermore, the proposed method has the advantage of improving pump performance by avoiding an increase in the initial priming volume and simplifying the design of the pump head flow path. However, the number of sensors has increased but the axial and tilt displacements can be monitored simultaneously.

VII. REDUCTION OF THE DATASET AND ECD SENSORS

A. DATASET FOR NN TRAINING REDUCTION

We reduced the data for NN training while maintaining the same wide range of rotor displacements and attitudes to reduce the data collection task and NN training time. The reduced variety of experimental condition types, coupled with decreased sampling frequency and time, contribute to a downsized dataset. Table 5 displays the decreased variety of experimental condition types of the dataset for NN training.

Other than the dataset, the remaining setting parameters for NN training remained unchanged. Table 6 lists the different datasets for NN training under various conditions. We input outputs from seven ECD sensors at varying rotational speeds into different NNs obtained from different datasets from Table 6 to estimate radial displacements and compared these with measurements obtained using radial ECD sensors for measurement accuracy evaluation. Figs.18 (a) and (b) show the measurement accuracy of RMSE using NNs trained by

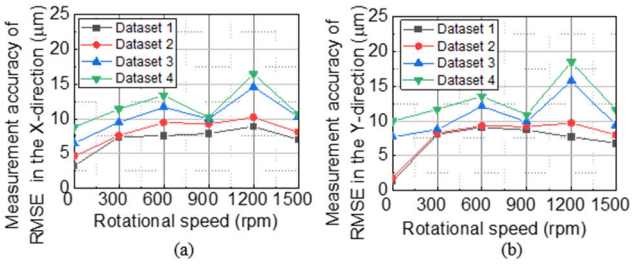

FIGURE 18. (a) Measurement accuracy of RMSE using NNs trained by different datasets in Table 6 at different rotational speeds in the X-direction; (b) Measurement accuracy of RMSE using NNs trained by different datasets in Table 6 at different rotational speeds in the Y-direction.

different datasets in Table 6 at different rotational speeds in the X- and Y-directions, respectively. It is obvious that datasets with greater numbers and diversity result in higher measurement accuracy.

After comparing the measurement accuracy of NNs, we proceeded with closed-loop feedback experiments based on the evaluated radial displacement using the NN trained by dataset 3 in Table 6. When the radial displacement obtained by the NN was used as the feedback signal, the rotor became unstable at startup. Stable suspension near the original position can be achieved by switching the feedback signals measured by the radial ECD sensors only at startup to the signals obtained using the NN near the origin.

The measured radial displacement during magnetic suspension at a speed of 900 rpm in the Y direction is shown in Fig. 19. The RMSEs between the radial ECD sensors and proposed sensor system were 13.6 and 12.8 μm in the X- and Y-directions, respectively, which is slightly larger than the previous error as shown in Table 4. However, the rotor experienced instability and failure when operated at higher rotational speeds owing to measurement errors.

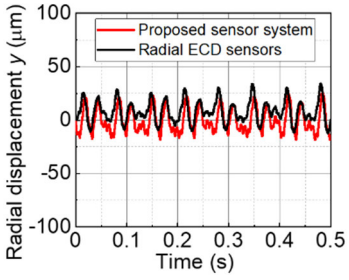

FIGURE 19. Measured radial displacement in the Y-direction during displacement feedback control based on the evaluated radial displacement using NN trained by dataset 3 in Table 6 at a speed of 900 rpm.

B. REDUCTION OF THE NUMBER OF ECD SENSORS

In principle, seven ECD sensors under the rotor can be reduced to five. Therefore, ECD sensors S_4 and S_7 were removed. For the NN training, the outputs from ECD sensors S_4 and S_7 were not used. The calculated MSE increased to

TABLE 5. Lists of the decreased variety of the experimental conditions types of the dataset for NN training.

Decreased variety of the experimental condition types of the dataset for NN training		
Types	Parameters	Positions and values
Magnetic suspension startup with different initial positions	Initial positions	Positive and negative directions of the Y-axis
Magnetic suspension with the different radial circular orbit targets	Amplitudes of several radial circular orbit targets [μm]	0/20/40/60/80/100
Magnetic suspension at different rotational speeds with the different radial circular orbit targets	Amplitudes of several radial circular orbit targets [μm]	0/10/20/30
	Rotational speeds [rpm]	100/500/900/1300/1700

TABLE 6. Lists of different datasets for NN Training under various conditions.

Datasets	1	2	3	4
Experimental condition types	Table 3	Table 3	Table 5	Table 5
Sampling frequency (Hz)	5000	100	5000	100
Sampling time (s)	3	1	3	1
Time response points	765000	5100	420000	2800
Final calculated MSE (μm^2)	60.3	80.4	91.6	121.1

179 μm^2 utilizing the same dataset 1 in Table 6, considerably higher than the previous MSE. Figs. 20 (a) and (b) show the measurement accuracy of RMSE using different sensor placements at different rotational speeds in the X- and Y-directions, respectively. With the same neural network structure, the measurement accuracy of RMSE of radial displacement using the seven-sensor placement surpasses the measurement accuracy achieved with the five-sensor placement due to sufficient input information.

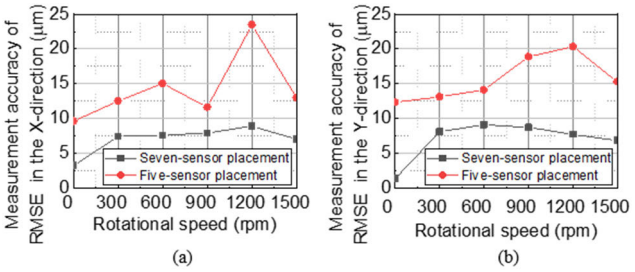

FIGURE 20. (a) Measurement accuracy of RMSE using different sensor placement at different rotational speeds in the X-direction; (b) Measurement accuracy of RMSE using different sensor placement at different rotational speeds in the Y-direction.

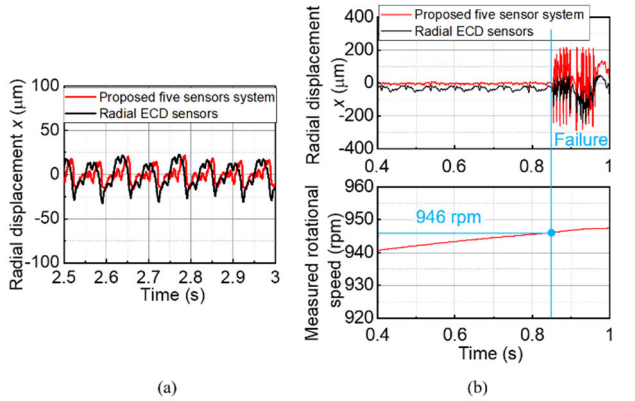

FIGURE 21. Displacement feedback control based on the evaluated radial displacement measured using the proposed five-sensor system: (a) Stable suspension at 900 rpm; (b) Failed suspension when further increasing rotational speed.

In the feedback experiment, magnetic suspension using this NN and five ECD sensor configurations failed. We increased the number of neurons in the hidden layer from 10 to 40 to enhance measurement accuracy and reliability. Consequently, the training time was tripled using the same dataset and the calculated MSE decreased to 72.3 μm^2.

The improved NN enables stable magnetic suspension at startup and during rotation. The measured radial displacements at a speed of 900 rpm in the X-direction, with an RMSE of 13.0 μm between the radial ECD sensors and the proposed five-sensor system are shown in Fig. 21 (a). However, the rotor became unstable when further increasing the rotational speed. The measured radial displacement and the corresponding rotational speed during the speed increase are shown in Fig. 21 (b). Besides, the magnetic suspension startup can be achieved with an error of 7.1 μm after reaching stability, as shown in Fig. 22. However, a large oscillation at startup was observed due to measurement error.

ECD sensors with differential placement methods improved the radial measurement accuracy with a simpler NN structure, avoiding measurement sensitivity reduction because the sensor target was far from the sensor probe and helped suppress signal noise and temperature drift.

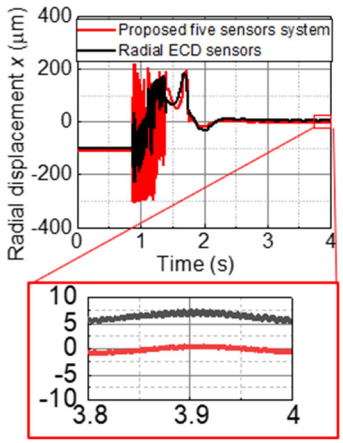

FIGURE 22. Measured radial displacement in the X-direction during displacement feedback control based on the evaluated radial displacement measured using the proposed five-sensor system during magnetic suspension startup.

C. DATASET CAPTURE IN THE COMMERCIAL APPLICATION FOR NN TRAINING

In our experiment, the dataset for NN training was captured using radial ECD sensors inside the rotor of the BELRSM to calibrate the ECD sensors under the rotor. However, this method for commercially available CBPs could not be used because the radial ECD sensors occupy the inner rotor space.

To solve this problem, we can use laser displacement meters mounted at the rotor outside to measure the radial displacement of the rotor instead of ECD sensors located inside the rotor. To obtain the dataset for NN training, we can remove commercially available pump-top housing in the absence of a working fluid and use hammering to introduce an impulse force on the rotor during suspension to simulate wider-range rotor motions and attitudes instead of the hydraulic force in the CBP.

VIII. CONCLUSION

This study presented a radial displacement measurement method in a BELRSM by mounting ECD sensors on the underside of the rotor's inner edge. The ECD sensor placement could prevent an increase in the rotor height and occupation of the inner side of the rotor space when ECD sensors were conventionally placed outside or inside the rotor. An arrangement of seven ECD sensors was proposed to compensate for the axial displacement, tilt angle, and nonlinear effects of the displacement-voltage characteristics of the sensors in radial displacement measurements. The relationship between the output voltages of the seven ECD sensors and radial displacement of the rotor was established using NN and backpropagation algorithms. The maximum errors of the proposed measurement linearity were 13.6 and 17.1 μm in the X- and Y-directions within the range of $\pm$150 μm, respectively. A measured bandwidth of 200 Hz was obtained. Additionally, radial displacement feedback control during magnetic suspension startup and rotation was successfully achieved, with RMSE within 16 μm. Employing more diverse and extensive datasets, along with a greater number of sensors, can offer richer information, leading to enhanced measurement accuracy. If the motions and attitudes of the rotor are not included in the dataset for NN training, significant measurement errors can occur. Further experimental investigations are necessary to assess the robustness of neural networks in such cases in the future.

ACKNOWLEDGMENT

The study is also contributed by Design and Manufacturing Division of Open Facility Center, Tokyo Institute of Technology.

REFERENCES

[1] T. Reichert, T. Nussbaumer, and J. W. Kolar, "Bearingless 300-W PMSM for bioreactor mixing," *IEEE Trans. Ind. Electron.*, vol. 59, no. 3, pp. 1376–1388, Mar. 2012.
[2] N. Kurita, T. Ishikawa, N. Saito, T. Masuzawa, and D. L. Timms, "A double-sided stator type axial bearingless motor development for total artificial heart," *IEEE Trans. Ind. Appl.*, vol. 55, no. 2, pp. 1516–1523, Mar. 2019.
[3] R. Yang, Z. He, N. Sugita, and T. Shinshi, "Low-cost and compact disposable extracorporeal centrifugal blood pump utilizing a homopolar bearingless switched reluctance slice motor," *IEEE Access*, vol. 11, pp. 24353–24366, 2023.
[4] F. Wang, Y. Zhu, H. Wang, and D. Zhao, "Design and analysis of a bearingless permanent-magnet motor for axial blood pump applications," *IEEE Access*, vol. 8, pp. 7622–7627, 2020.
[5] J. Rao, W. Hijikata, and T. Shinshi, "A bearingless motor utilizing a permanent magnet free structure for disposable centrifugal blood pumps," *J. Adv. Mech. Des., Syst., Manuf.*, vol. 9, no. 3, 2015, Art. no. JAMDSM0046.
[6] D. Steinert, T. Nussbaumer, and J. W. Kolar, "Slotless bearingless disk drive for high-speed and high-purity applications," *IEEE Trans. Ind. Electron.*, vol. 61, no. 11, pp. 5974–5986, Nov. 2014.
[7] Z. Liu, A. Chiba, Y. Irino, and Y. Nakazawa, "Optimum pole number combination of a buried permanent magnet bearingless motor and test results at an output of 60 kW with a speed of 37000 r/min," *IEEE Open J. Ind. Appl.*, vol. 1, pp. 33–41, 2020.
[8] J. Chen, J. Zhu, and E. L. Severson, "Review of bearingless motor technology for significant power applications," *IEEE Trans. Ind. Appl.*, vol. 56, no. 2, pp. 1377–1388, Mar. 2020.
[9] R. Schoeb and N. Barletta, "Magnetic bearing. Principle and application of a bearingless slice motor," *JSME Int. J. Ser. C*, vol. 40, no. 4, pp. 593–598, 1997.
[10] R. Schöb, N. Barletta, and J. Hahn, "The bearingless centrifugal pump—A perfect example of a mechatronics system," *IFAC Proc. Volumes*, vol. 33, no. 26, pp. 443–448, Sep. 2000.
[11] B. S. Weinreb, M. Noh, D. C. Fyler, and D. L. Trumper, "Design and implementation of a novel interior permanent magnet bearingless slice motor," *IEEE Trans. Ind. Appl.*, vol. 57, no. 6, pp. 6774–6782, Nov. 2021.
[12] T. Holenstein, M. Schuck, and J. W. Kolar, "Performance benchmarking of a novel magnet-free bearingless synchronous reluctance slice motor," *IEEE Open J. Ind. Electron. Soc.*, vol. 1, pp. 184–193, 2020.
[13] B. Wex, A. Zochbauer, H. Mitterhofer, and W. Gruber, "Topology comparison and design of a slotted bearingless high-speed permanent magnetic synchronous machine," in *Proc. IEEE Int. Electr. Mach. Drives Conf. (IEMDC)*, San Diego, CA, USA, May 2019, pp. 1–8.
[14] J. Asama, D. Kanehara, T. Oiwa, and A. Chiba, "Performance investigation of a centrifugal pump with a consequent-pole bearingless motor," in *Proc. IEEE Energy Convers. Congr. Expo. (ECCE)*, Raleigh, NC, USA, Sep. 2012, pp. 3663–3669.
[15] T. Pei, D. Li, J. Liu, and W. Kong, "A novel flux-reversal bearingless slice motor controlled by rotor angle independent suspension current," *IEEE Trans. Ind. Electron.*, vol. 70, no. 6, pp. 5615–5625, Jun. 2023.
[16] M. Noh and D. L. Trumper, "Homopolar bearingless slice motor with flux-biasing Halbach arrays," *IEEE Trans. Ind. Electron.*, vol. 67, no. 9, pp. 7757–7766, Sep. 2020.

[17] W. Gruber, W. Briewasser, M. Rothböck, and R. T. Schöb, "Bearingless slice motor concepts without permanent magnets in the rotor," in *Proc. IEEE Int. Conf. Ind. Technol. (ICIT)*, Cape Town, South Africa, Feb. 2013, pp. 259–265.
[18] G. He, J. Zhang, A. Shah, Z. B. Berk, L. Han, H. Dong, B. P. Griffith, and Z. J. Wu, "Flow characteristics and hemolytic performance of the new breethe centrifugal blood pump in comparison with the CentriMag and rotaflow pumps," *Int. J. Artif. Organs*, vol. 44, no. 11, pp. 829–837, Nov. 2021.
[19] H. Hoshi, J. Asama, W. Hijikata, C. Hara, T. Shinshi, T. Yasuda, K. Ohuchi, A. Shimokohbe, and S. Takatani, "Hemolytic performance of a MagLev disposable rotary blood pump (MedTech Dispo): Effects of MagLev gap clearance and surface roughness," *Artif. Organs*, vol. 30, no. 12, pp. 949–954, Dec. 2006.
[20] D. Luenberger, "An introduction to observers," *IEEE Trans. Autom. Control*, vol. AC-16, no. 6, pp. 596–602, Dec. 1971.
[21] T. Mizuno, K. Araki, and H. Bleuler, "Stability analysis of self-sensing magnetic bearing controllers," *IEEE Trans. Control Syst. Technol.*, vol. 4, no. 5, pp. 572–579, Sep. 1996.
[22] Y. G. Kang, D. Fernandez, and D. D. Reigosa, "Saliency-based rotor spatial position displacement self-sensing for self-bearing machines," *Sensors*, vol. 22, no. 24, p. 9663, Dec. 2022.
[23] Y. Kato, T. Yoshida, and K. Ohniwa, "Self-sensing active magnetic bearings with zero-bias-current control," *IEEJ Trans. Ind. Appl.*, vol. 126, no. 10, pp. 1399–1405, 2006.

REN YANG was born in Huaihua, Hunan, China, in 1994. He received the B.S. degree in mechanical engineering from the Dalian University of Technology, China, in 2017, and the M.S. degree in mechanical engineering from the Tokyo Institute of Technology, Japan, in 2019, where he is currently pursuing the Ph.D. degree in mechanical engineering. His research interests include magnetic bearing and bearingless motors.

ZEQIANG HE (Graduate Student Member, IEEE) was born in Hangzhou, Zhejiang, China, in 1997. He received the B.S. degree in electrical engineering from Zhejiang University, China, in 2020, and the M.S. degree in mechanical engineering from the Tokyo Institute of Technology, Japan, in 2022, where he is currently pursuing the Ph.D. degree in mechanical engineering. His research interests include the development of the bearingless motor and its application in the blood pump.

NAOHIRO SUGITA received the B.S., M.S., and Ph.D. degrees in mechanical engineering from Keio University, Yokohama, Japan, in 2012, 2014, and 2017, respectively. From 2017 to 2019, he was a Researcher with the Products Development Center, IHI Corporation, Yokohama. Since 2019, he has been an Assistant Professor with the Laboratory for Future Interdisciplinary Research of Science and Technology, Tokyo Institute of Technology. His research interests include mechanical and acoustic resonances, nonlinear vibration, ultrasound cavitation, bubble oscillations in an ultrasound field, and medical ultrasound applications.

TADAHIKO SHINSHI (Member, IEEE) received B.E., M.E., and Dr.-Eng. degrees from the Tokyo Institute of Technology, Japan, in 1990, 1992, and 2000, respectively. From 1992 to 1995, he was with the Mechanical Engineering Research Laboratory, Hitachi Ltd. In 1995, he joined the Precision and Intelligence Laboratory (P&I Lab.), Tokyo Institute of Technology, as a Research Associate and became an Associate Professor and a Professor, in 2000 and 2010, respectively. He is currently with the Institute of Innovation Research (IIR), Tokyo Institute of Technology, as a Professor. His current research interests include micro-mechatronics and precision motion control.